



The Geologic Impact of 16 Psyche's Surface Temperatures

Carver J. Bierson , Linda T. Elkins-Tanton , and Joseph G. O'Rourke
School of Earth and Space Exploration, Arizona State University, Tempe, AZ, USA; CBierson@asu.edu
Received 2022 January 4; revised 2022 July 19; accepted 2022 July 22; published 2022 August 18

Abstract

NASA's Discovery mission Psyche will soon be launched to visit the asteroid 16 Psyche. In this work, we model the surface temperatures of 16 Psyche. Our modeling is focused on capturing the diurnal and seasonal surface temperature variations caused by 16 Psyche's large obliquity (95°) and moderately high eccentricity (0.134). Using a semianalytic framework, we predict that large thermal variations (including at the poles) can cause cracking of boulders leading to a porous surface regolith. This prediction is consistent with a high-porosity surface regolith inferred from thermal inertia measurements. We also find that water ice is not likely to be stable at any latitude.

Unified Astronomy Thesaurus concepts: Asteroid surfaces (2209); Asteroids (72)

1. Introduction

The Psyche spacecraft will soon be launched to visit the asteroid 16 Psyche (hereafter called Psyche). Psyche was previously thought to be a nearly completely metallic world, although more recent observations have suggested it may be a metal–silicate mixture (Elkins-Tanton et al. 2020). Regardless of composition, Psyche's surface temperatures have a large impact on the material properties of the surface, including thermal properties (Opeil et al. 2010; Wood 2020), the deformation style during impacts (Marchi et al. 2020), and the volatile content of that surface (Schorghofer 2008). Therefore, characterizing the range of plausible surface temperatures is important for many premission analyses. In this work, we model Psyche's surface temperatures with a particular focus on constraining the expected variation and the impact those temperatures have on the surface.

Psyche has an extreme obliquity of ~95° (Shepard et al. 2017). High-obliquity worlds experience a unique climate regime. On Earth and other low-obliquity worlds, the equatorial tropics receive periods of directly overhead insolation. In contrast, the poles experience alternating periods of constant darkness or daylight. On Earth, polar insolation (the amount of incoming solar radiation) is always muted because the Sun is low in the sky (less than 23° above the horizon). On high-obliquity worlds, most of the surface experiences both periods of direct overhead insolation and extended periods of darkness.

The key thermal properties that control heat transfer in a planetary surface are the thermal conductivity (k), density (ρ), and specific heat (c_p). These are often grouped into the thermal diffusivity given by

$$\kappa = \frac{k}{\rho c_p}. \quad (1)$$

While κ describes the thermal diffusion in the subsurface, the cooling time of the surface is more directly related to an alternative grouped parameter, thermal inertia

(Spencer et al. 1989):

$$\Gamma = \sqrt{k\rho c_p}. \quad (2)$$

The SI units for thermal inertia are $\text{J m}^{-2} \text{K}^{-1} \text{s}^{-1/2}$, which we will refer to as tiu (Putzig 2006).

For Psyche, three independent estimates of thermal inertia have been determined (Matter et al. 2013; Landsman et al. 2018; de Kleer et al. 2021). All of these studies used a combination of telescopic observations (either infrared or radio) and thermal modeling. With their 1σ uncertainties, their preferred estimates are 123 ± 50 (Matter et al. 2013), 15 ± 10 (Landsman et al. 2018), and 280 ± 100 tiu (de Kleer et al. 2021; Cambioni et al. 2022). Of these preferred estimates, only Matter et al. (2013) and de Kleer et al. (2021) slightly overlap at 1σ , although Landsman et al. (2018) also presented some retrievals that yield estimates of ~100–200 tiu. Ultimately, measurements of thermal inertia require complex observations, and retrievals depend on assumptions about, for example, the surface emissivity and size and shape of Psyche. In this work, we do not attempt to reconcile these estimates but instead characterize the surface temperatures over a wide range of thermal inertia values.

Thermal modeling of asteroids serves a wide range of goals. Previous thermal models have been used to determine asteroid diameters (Spencer et al. 1989), characterize the impact of radiation on spin rate (YORP effect; Vokrouhlický et al. 2015), quantify thermal fatigue (Delbo et al. 2014), predict volatile stability (Schorghofer 2016), and constrain thermal properties (Delbo et al. 2015). Each of these goals requires models of differing scales and resolutions. Previous models for Psyche have focused on retrieving the surface thermal inertia (Matter et al. 2013; Landsman et al. 2018; de Kleer et al. 2021). To this end, these models have focused on replicating the surface temperatures on the observed face at the time the observations were made. In this work, we model diurnal and annual temperature variations at all latitudes to characterize their impact on the surface itself.

Thermal stresses have been suggested to drive crack propagation on many asteroids. On Bennu, this has been suggested to play an important role in causing centimeter-scale particles to be ejected from the surface (Molaro et al. 2020). Previous studies used finite element modeling to characterize the crack propagation rate under different conditions (Delbo et al. 2014; Molaro et al. 2017; El Mir et al. 2019). In all cases, these works focused on the impact of diurnal temperature



Original content from this work may be used under the terms of the [Creative Commons Attribution 4.0 licence](https://creativecommons.org/licenses/by/4.0/). Any further distribution of this work must maintain attribution to the author(s) and the title of the work, journal citation and DOI.

variations (Hamm et al. 2019). Here we use a semianalytic theory to compare the relative importance of diurnal and annual thermal stresses for Psyche.

In this work, we first describe the thermal model used and our choice of parameters. In Section 3, we characterize the range of plausible temperatures and temperature variations at Psyche's surface. We then consider the implications of our model on volatile retention and regolith production via thermal cracking.

2. Model Description

We developed a thermal model to solve for the surface temperature of Psyche. Because from the Earth, Psyche is always viewed a low phase angle, previous models were configured to accurately reproduce dayside temperatures. Modeling daytime temperatures only requires resolving the diurnal thermal wave (including thermal emission from the nightside); accordingly, these models simulate much less than one orbit at a time (Matter et al. 2013; Landsman et al. 2018). The goal of this work is to resolve surface temperatures at all times in Psyche's orbit at all locations on the surface. To accurately predict surface temperatures in polar winter, the model must capture both diurnal and seasonal thermal waves. For this reason, we use a model setup similar to Kieffer (2013) and MacLennan et al. (2021). A more detailed comparison of this model with other configurations is presented in Appendix C.1.

To calculate the instantaneous solar insolation for each location on the surface, S , we use the JPL SPICE package (Acton et al. 2016; Annex et al. 2020). The SPICE toolkit determines the distance from Psyche to the Sun and the location of the Sun in Psyche's body-fixed reference frame. The solar insolation is then given by

$$S = S_0 \left(\frac{1}{d^2} \right) \max(0, N \cdot \hat{S}), \quad (3)$$

where S_0 is the solar constant at 1 au, d is Psyche's instantaneous distance from the Sun in AU, N is the local surface normal vector, and \hat{S} is the unit vector from the center of Psyche to the Sun in the Psyche-fixed reference frame.

In this work, we use the shape model from Shepard et al. (2017).¹ Given the wide range in thermal properties to explore, we are not analyzing the longitudinal variations in temperature caused by the shape. While local features will cause some lateral temperature variations, Psyche's high obliquity eliminates the possibility of polar permanently shadowed regions as seen on the Moon and Mercury (Watson et al. 1961; Paige et al. 1992). As such, the shape model is averaged at each latitude by calculating the surface normal vectors, N , across the surface in the Psyche body. At each latitude, we then use the mean of N_z and $\sqrt{N_x^2 + N_y^2}$.

At each time step, the model determines the surface temperature and then solves the 1D heat diffusion equation,

$$\rho c_p \frac{dT}{dt} = -\frac{d}{dz} \left(k \frac{dT}{dz} \right). \quad (4)$$

We follow the discretization of the thermal diffusion equation by Kieffer (2013). This discretization properly

handles changes in the layer thickness and thermal conductivity with depth:

$$\Delta T_i = F_{1i}[T_{i+1} + F_{2i}T_i + F_{3i}T_{i-1}], \quad (5)$$

$$F_1 = \frac{2\Delta t}{\Delta z_i \rho_i c_{pi}} \left(\frac{1}{\frac{\Delta z_i}{k_i} + \frac{\Delta z_{i+1}}{k_{i+1}}} \right), \quad (6)$$

$$F_3 = \left(\frac{\Delta z_i}{k_i} + \frac{\Delta z_{i+1}}{k_{i+1}} \right) \left(\frac{1}{\frac{\Delta z_i}{k_i} + \frac{\Delta z_{i-1}}{k_{i-1}}} \right), \quad (7)$$

$$F_2 = -(1 + F_3). \quad (8)$$

The discretization shown in Equation (5) is then used in a fully implicit solver. At the upper model boundary, Psyche's surface, the temperature is held fixed. At the lower boundary, we apply a zero-flux boundary condition. Here superscripts refer to the time index, and subscripts refer to the spatial index:

$$AT^{j+1} = T^j, \quad (9)$$

$$T^{j+1} = A^{-1}T^j, \quad (10)$$

$$A = \begin{pmatrix} 1 & 0 & 0 & 0 & \cdots & 0 \\ F_{1,2} & F_{2,2} & F_{3,2} & 0 & \cdots & 0 \\ 0 & \ddots & \ddots & \ddots & 0 & 0 \\ 0 & \cdots & 0 & F_{1,n-1} & F_{2,n-1} & F_{3,n-1} \\ 0 & \cdots & 0 & 0 & -F_{1,n} & 1.0 + F_{1,n} \end{pmatrix}. \quad (11)$$

One advantage of this technique is that, so long as the thermal conductivity is temperature-independent, the matrix A is constant and so only needs to be inverted once. All subsequent diffusion calculations are then just a matrix multiplication operation, greatly improving speed.

The surface temperature is considered constant for the above diffusion step. At the start of each time step, the surface temperature is independently updated by solving

$$\rho c_p \Delta z \frac{dT}{dt} \Big|_{z=0} = (1 - A)S - \epsilon \sigma_{SB} T_{z=0}^4 - k \frac{dT}{dz} \Big|_{z=0}, \quad (12)$$

where A is the Bond albedo, ϵ is the thermal emissivity, σ_{SB} is the Stefan-Boltzmann constant, and Δz is the layer thickness at the surface. We do not include an additional term for surface roughness, which is equivalent to assuming a smooth surface. A smooth surface was found to be the best fit to existing observational data (Matter et al. 2013; Landsman et al. 2018; de Kleer et al. 2021). The broad range of thermal inertia explored also has a similar effect to adding uncertainty in surface roughness (see review in Delbo et al. 2015).

The key length scale in a cyclically forced thermal diffusion system is the thermal skin depth. The thermal skin depth is the e-folding scale over which surface temperature variations decay to the annual mean temperature. For a given forcing period, P , the skin depth is given by Turcotte & Schubert (2014):

$$\delta = \sqrt{\frac{P\kappa}{\pi}} = \frac{\Gamma}{\rho c_p} \sqrt{\frac{P}{\pi}}. \quad (13)$$

Psyche has two dominant periods, its rotation of 4.2 hr and its orbit of 5.0 yr (Shepard et al. 2021), and therefore two thermal skin depths. The difference between these periods leads to the

¹ The new shape model of Shepard et al. (2021) does resolve more detailed features. The long-wavelength shape, important for this work, is largely unchanged.

annual skin depth being ~ 100 times deeper than the diurnal skin depth (assuming constant thermal properties with depth).

The vertical grid in this model must both have a fine resolution in the near surface to resolve the diurnal thermal wave and reach several seasonal skin depths deep for the seasonal thermal wave. To resolve both of these scales while keeping the total number of points modest, the grid spacing is initially constant for the first N_{surf} grid cells. The cells then grow in size linearly until the last cell is $\Delta z = 2z_{\text{max}}/N$, where N is the total number of grid cells. For the results shown, we use an initial layer thickness of $1/10$ of the diurnal skin depth, z_{max} is eight seasonal skin depths, $N_{\text{surf}} = 10$, and $N = 50$.

To initialize the model, we start from a constant temperature with depth. After one full orbit, at each cell, the mean temperature is calculated, and the temperature profile is reset to that mean value at all depths. The model is then run for three more orbits to initialize the seasonal thermal wave. Only after this point are results recorded. This approach allows for the difference in mean annual temperature with thermal inertia (discussed in Section 3) to be directly evaluated and provides the model sufficient time to initialize the annual thermal wave. Running the model for longer can cause minor changes in the temperature at the base of the model (< 5 K) but has no notable impact on the surface temperatures, the focus of this study. An evaluation of the model accuracy with this configuration is presented in Appendix C.

3. Model Results

Figure 1 shows the typical output from one of our model runs for each pole and the equator. Panel (c) shows the temperatures over a year. The thickness of the lines is due to diurnal temperature variations. The poles experience no diurnal cycle and so have a nearly constant temperature gradient in the upper annual skin depth (~ 1 cm).

In addition to high obliquity, Psyche also has significant eccentricity. The combined impact is that one pole (the south) experiences more summer isolation than the other but for a shorter period of time. The mean insolation experienced by both poles over the whole year is the same (Ward 1974; Dobrovolskis 2021). However, because the surface temperature is not linear with surface isolation, the mean temperatures are not the same at both poles. Figure 2 shows how the mean temperature at each latitudinal band depends on latitude and thermal inertia.

Our model predicts that Psyche's poles have a difference in mean temperature of about 20 K with a larger difference for lower thermal inertia. The mean temperatures are higher in the northern hemisphere, which experiences a longer but weaker polar summer. The southern latitudes experience a larger temperature contrast (Figure 2(b)) with a warmer and shorter local summer.

3.1. Water Ice Stability

On airless bodies, the stability of water ice is controlled by the temperature and the ease with which a gas molecule can diffuse to the surface, which scales with the vapor pressure (Schorghofer 2016; Rozitis et al. 2020). Because vapor pressure is exponential with temperature, there is a near step function behavior where below a critical temperature, ice is stable and above which it is rapidly lost. At the surface, water ice at temperatures ≤ 100 K is indefinitely stable

(Schorghofer & Taylor 2007). With 10 cm of regolith cover, ice at 120 K can be stable (Schorghofer & Taylor 2007). At temperatures above 145 K, ice is not stable even with meters of cover (Schorghofer 2008).

From this work, the maximum surface temperatures at all latitudes reach > 200 K, clearly removing any ice from the upper diurnal skin depths. Only in the southern polar region are mean annual temperatures below 145 K (Figure 2). Depending on the diffusivity of the overlying regolith, ice buried > 3 m (several seasonal skin depths) may be stable for as short as thousands of years or as long as the age of the solar system (Schorghofer & Hsieh 2018). However, as discussed in Section 4, precession of the spin axis will eventually cause the southern pole to warm, removing any chance for permanently stable water ice. This model result is consistent with the lack of observed water ice spectral features in the UV (Becker et al. 2020).

3.2. Thermal Cracking

Given the large seasonal temperature variation predicted by this thermal model (Figure 2), we now consider the impact the resulting thermal stresses may have on Psyche's surface. Recent numerical and laboratory work has demonstrated the importance of thermal cycling in regolith development on airless bodies (Delbo et al. 2014; Molaro et al. 2017; Hazeli et al. 2018; El Mir et al. 2019; Libourel et al. 2021). This work has primarily focused on thermal forcing from diurnal cycles, the dominant thermal forcing for most of the surface on low-obliquity worlds. However, on Psyche and other high-obliquity objects, the annual temperature contrasts are more than an order of magnitude larger than their diurnal counterparts over most of the surface (Figure 1).

We can use an analytic scaling to estimate the timescales over which thermal stresses would fracture surface boulders. We apply the empirical Paris law (Janssen et al. 2002),

$$\frac{da}{dN} = C(\Delta K)^m, \quad (14)$$

where a is the crack length, N is the number of cycles, ΔK is the crack tip stress intensity, and C and m are empirically determined constants.

Neglecting elastic forces, ΔK , can be related to the tensile stress opening the crack by (Janssen et al. 2002; Collins & Stock 2016),

$$\Delta K \approx \Delta \sigma \sqrt{\pi a}, \quad (15)$$

where a is the crack length, and $\Delta \sigma$ is the stress variation. If $\Delta \sigma$ is independent of a , we can integrate Equation (14) (shown in Appendix D) to

$$a(N) = [(1 - m/2)C(\Delta \sigma \sqrt{\pi})^m N + a_0^{1-m/2}]^{1/(1-m/2)}. \quad (16)$$

We can define a critical number of cycles at which the behavior changes as

$$N_{\text{crit}} = \frac{-a_0^{1-m/2}}{(1 - m/2)C(\Delta \sigma \sqrt{\pi})^m}. \quad (17)$$

Substituting N_{crit} into Equation (16) gives

$$a(N) = a_0 \left[1 - \frac{N}{N_{\text{crit}}} \right]^{1/(1-m/2)}. \quad (18)$$

2026 FEB 04

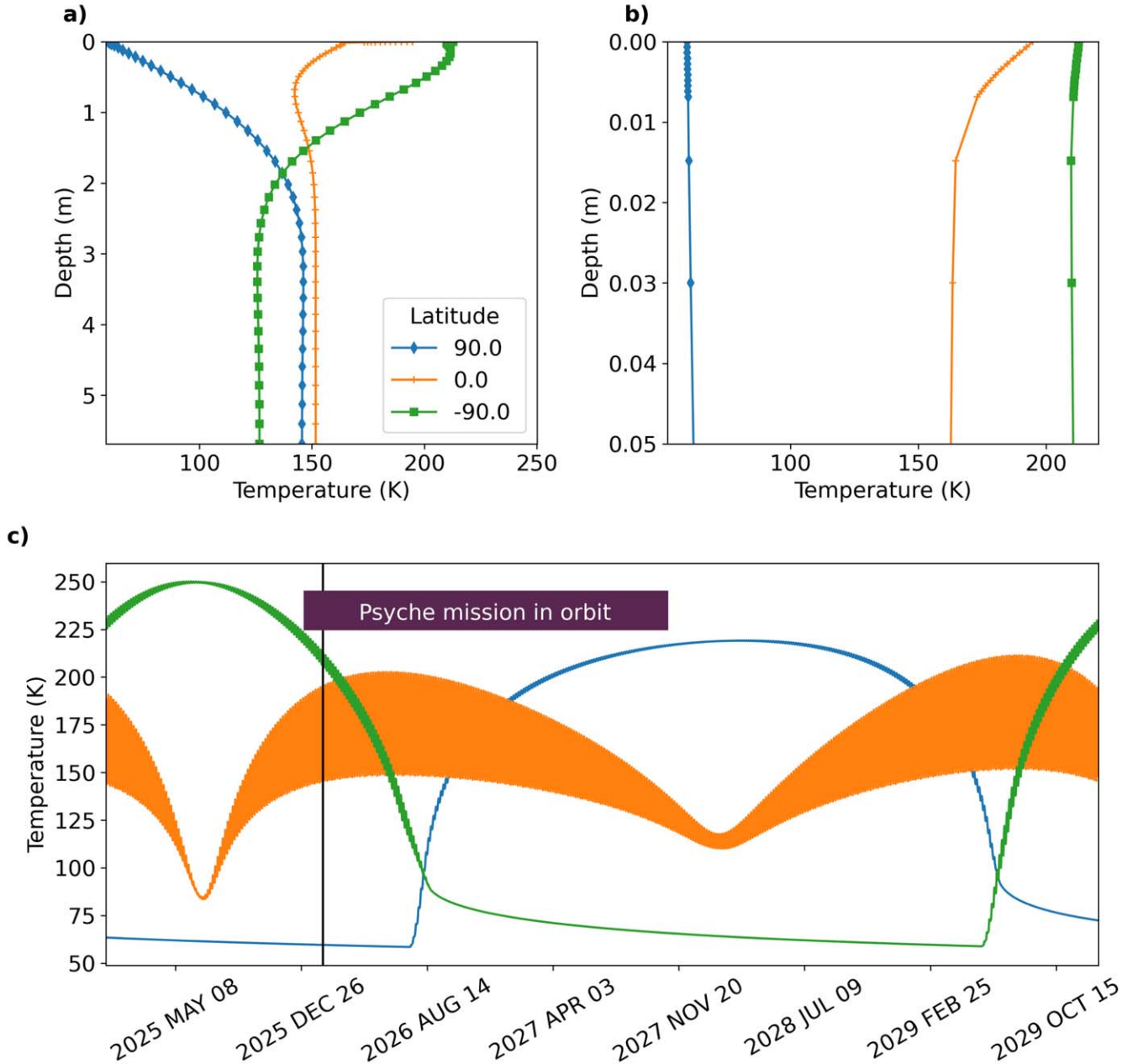


Figure 1. Example of typical model output. Temperatures are shown at the equator and each pole using thermal parameters corresponding to 100 tiu ($k = 0.01 \text{ W m}^{-1} \text{ K}^{-1}$, $\rho = 2000 \text{ kg m}^{-3}$, $c_p = 500 \text{ J kg}^{-1}$). Panels (a) and (b) show temperatures with depth at the same time snapshot. Panel (b) is a zoom-in of the top 5 cm of panel (a) to emphasize the diurnal skin depth. Symbols are placed at model cell centers. Panel (c) shows the surface temperature over 1 Psyche yr. The thickness of the lines is due to the day–night temperature variations. The vertical black line corresponds to the time of panels (a) and (b).

This equation has two important regimes. When $N \ll N_{\text{crit}}$, the crack grows very slowly ($a(N) \approx a_0$). As the number of cycles approaches N_{crit} , the crack grows as a power law, quickly leading to total failure. Because of this rapid crack growth, so long as the host rock is much larger than the initial crack size, it will always take roughly N_{crit} cycles to fully fracture. This behavior is observed in experimental studies of the crack growth of marble samples (Migliazza et al. 2011) and shown in Figure 10.

To apply this to Psyche, we must make a rough estimate of the tensile stress variation, $\Delta\sigma$. There are two physical causes

for this stress, sometimes described by the terms microscopic and macroscopic stress (Ravaji et al. 2019). Both of these stress terms arise from differential thermal expansion within the host rock. Microscopic stress arises from grains having different thermal expansivity. This stress is maximized when there are large temperature changes and large differences in the thermal expansivity between grains. Macroscopic stresses arise from the temperature gradient within the host rock. For this reason, stress is maximized when the host rock is similar in size to the thermal skin depth (Molaro et al. 2017; El Mir et al. 2019; Ravaji et al. 2019).

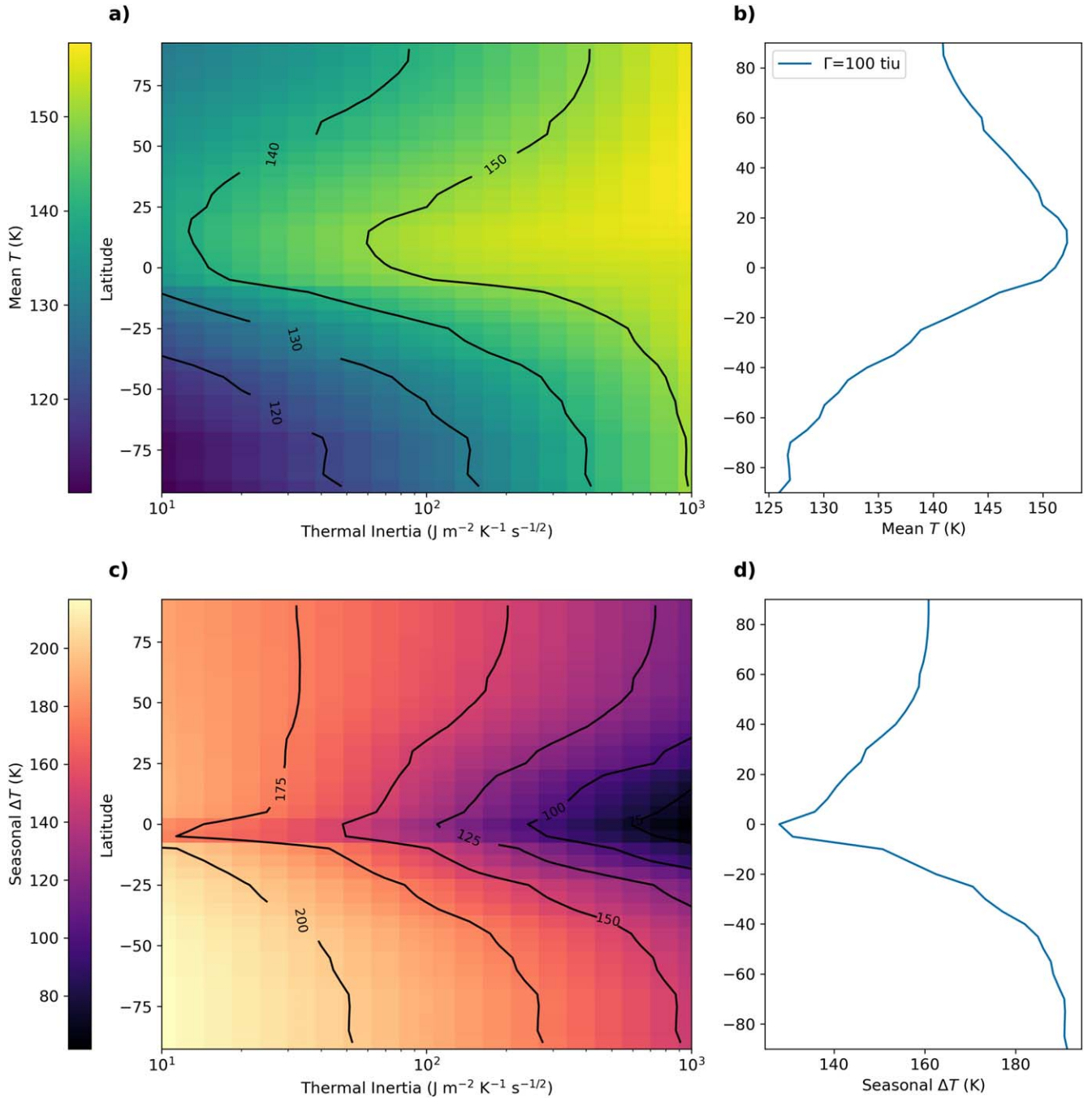


Figure 2. Annual temperature variations exceed 100 K over nearly all of Psyche’s surface over a wide of thermal inertia values. In the southern hemisphere, the mean temperatures are consistently lower, while the temperature variations are larger. (a) Annual mean temperature as a function of latitude and thermal inertia (Γ). (b) One profile from panel (a) for a thermal inertia of 126 tiu (same as Figure 1). This thermal inertia is a representative value chosen to show the north–south differences. (c) Difference between the local minimum surface temperature and maximum surface temperature within one Psyche orbit. (d) One profile from panel (c) for a thermal inertia of 100 tiu. For all panels, the specific heat and density are held constant ($c_p = 500 \text{ J kg}^{-1}$, $\rho = 2000 \text{ kg m}^{-3}$), while the thermal conductivity is varied.

To first order, both of these effects can be estimated by the thermal strain ($\alpha\Delta T$) multiplied by the elastic modulus (E). Thus, the stress is given by

$$\sigma \approx E\alpha\Delta T. \quad (19)$$

Substituting in the seasonal temperature variations (Figure 2) and characteristic silicate values,

$$\sigma \approx 50 \text{ MPa} \left(\frac{E}{50 \text{ GPa}} \right) \left(\frac{\alpha}{10^{-5} \text{ K}^{-1}} \right) \left(\frac{\Delta T}{100 \text{ K}} \right). \quad (20)$$

Because this estimate ignores elastic forces, we treat Equation (19) as an upper bound on the tensile stress variation.

Combining Equations (17) and (19) shows a scaling of $N_{\text{crit}} \propto (\alpha\Delta T)^{-m}$. This scaling is similar to that derived by El Mir et al. (2019). El Mir et al. (2019) fit their numerical experiments with an assumed linearized stress intensity of $\Delta K = \bar{A}a + \bar{B}$, where \bar{A} and \bar{B} are empirical constants, in place of the square-root scaling described by Equation (15). Thus, El Mir et al. (2019) found a scaling of $N_{\text{crit}} \propto (\alpha\Delta T)^{1.5(1-m)}$ when the rock is smaller than the skin depth.

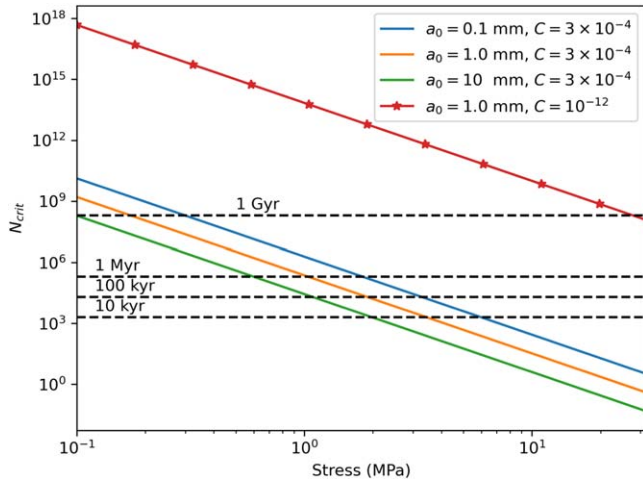


Figure 3. Thermal fracture is likely an important process on Psyche’s surface. The timescale of cracking will depend on the magnitude of the elastic forces countering thermal stress. The Paris law coefficient of $C = 10^{-12}$ m [MPa $\sqrt{\text{m}}]^{-m}$ is from industrially produced metals and so is unlikely to be representative of Psyche’s surface material. Horizontal dashed lines are the number of Earth years needed to reach that number of seasonal cycles, and a_0 is the initial crack size.

To estimate the cracking timescale requires estimates for the empirical parameters C and m . Delbo et al. (2014) found that values for C and m measured on Carrara marble produce a good fit to crack propagation in both ordinary and carbonaceous chondrites ($C = 3 \times 10^{-4}$ m [MPa $\sqrt{\text{m}}]^{-m}$, $m = 3.84$). These values are the mean of two measurements from the work of Migliazza et al. (2011). Those two measurements are $C = 3.7 \times 10^{-4}$ m [MPa $\sqrt{\text{m}}]^{-m}$, $m = 4.37$ and $C = 2.0 \times 10^{-4}$ m [MPa $\sqrt{\text{m}}]^{-m}$, $m = 3.42$. No similar measurements have been made on metallic meteorites. Industrially produced metals often have values of $C = 10^{-10}$ – 10^{-12} m [MPa $\sqrt{\text{m}}]^{-m}$ and $m \sim 4.0$ (Janssen et al. 2002). Industrial metals are likely poor analogs, however, since these materials are specifically engineered to resist crack propagation. Given that Psyche’s surface is unlikely to be pure metal (Elkins-Tanton et al. 2020; de Kleer et al. 2021), we speculate that the meteorite estimates are better analogs.

We can apply Equations (17) and (19) to address both the longevity of surface rocks and the relative impact of seasonal and diurnal forcing. Figure 3 shows N_{crit} as a function of the initial crack size and stress variation. Timescales are estimated assuming annual cycling (discussed more below). For material properties corresponding to chondritic material (Delbo et al. 2014) and thermal stresses of ~ 1 MPa, thermal cycling will cause full failure on a timescale of less than 1 Myr. In the other extreme, if we assume similar stresses but material properties measured for industrial metals ($C = 10^{-12}$ m [MPa $\sqrt{\text{m}}]^{-m}$; Janssen et al. 2002; Haddar et al. 2005), the surface material will not crack even over billions of years.

While it is difficult to determine the exact timescale of crack propagation given these material uncertainties, we can more directly compare the relative importance of diurnal and annual thermal forcing. We calculate the stress following Equation (19) with either the annual or diurnal temperature variation. Because the diurnal temperature variations change seasonally, we do not directly apply Equation (17) but instead numerically integrate Equation (14) until the crack grows to 1 m. More details and validation for this integration are provided in Appendix E.

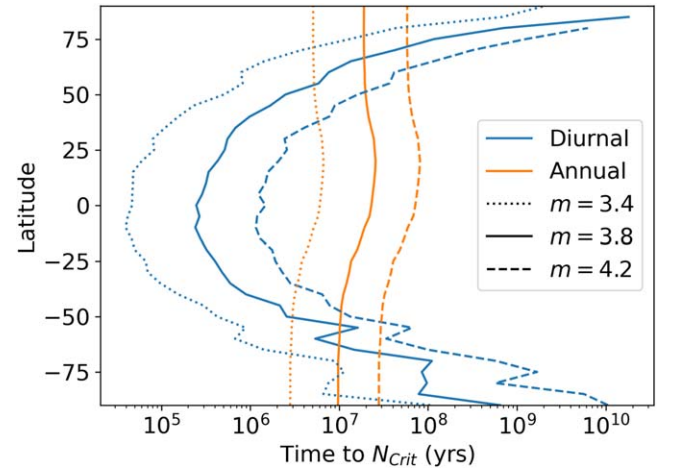


Figure 4. Depending on the Paris law exponent, m , seasonal temperature variations may be more important than diurnal variations in crack propagation for much of Psyche’s surface. Shown are the estimated time to full crack (N_{crit}^P) for diurnal and annual temperature variations as a function of latitude. For this calculation, $\Delta\sigma = fE\alpha\Delta T$, where $f = 0.01$. Changes in the assumed values of f , C , or a_0 would shift the timescale of both the annual and diurnal curves equally.

To account for the roughly 10^4 rotations in each Psyche orbit, we convert the N_{crit} values to a time to crack in years by multiplying by the appropriate period. Comparing the cracking timescale for these two periods does require assumed values of C and a_0 , although so long as those values are the same for both periods, the relative importance of the periods will not change. Changes in the value of m do change the relative importance, and thus three values of m are shown.

We find that for high latitudes, where the annual temperature variation is largest and temperature variations are smallest, those annual variations have a shorter time to fracture. The transition between these is strongly dependent on the exponent of the Paris law, m . For the nominal value of $m = 3.84$, this transition occurs at $\sim 65^\circ$ latitude, implying that on $\sim 10\%$ of the surface area, annual periods may dominate over diurnal ones.

What is not captured by Figure 4 is the differences in process between the annual and diurnal waves. The diurnal thermal forcing in very comparable to that studied in previous works where macroscopic stresses (from internal thermal gradients) dominate (Molaro et al. 2017; El Mir et al. 2019). This diurnal forcing will most efficiently fracture rocks with a size comparable to the skin depth of ~ 1 cm. The annual forcing, with its skin depth of ~ 1 m, will preferentially fracture larger rocks. However, the larger temperature variation in the annual wave will also amplify microscopic stresses (coming from intergranular variations in thermal expansivity). If Psyche’s surface is a mixture of metals and silicates, as has been hypothesized (Johnson et al. 2020), the large difference in thermal expansivity between those components could cause fracturing of rocks across a much broader size range. More detailed modeling would be needed to investigate how these micro- and macroscopic stresses would interact and the impact this would have on the surface rock size distribution.

4. Discussion

One of the biggest questions regarding Psyche is its composition. Many data sets have been brought to bear, most implying that Psyche is some metal–silicate mixture

(Elkins-Tanton et al. 2020; de Kleer et al. 2021). Of most relevance to this work are the thermal inertia measurements (summarized in the Introduction). In Appendix B, we describe in detail the relationship between thermal inertia, composition, and porosity. In summary, all of the existing thermal inertia estimates favor a high surface porosity ($>50\%$). However, because of the large uncertainty in the surface porosity, the thermal inertia estimates do not provide a strong constraint on composition.

Through this work, we examine the role of diurnal and seasonal temperature variations on Psyche's surface temperatures. These are driven by Psyche's current orbit and spin configuration. However, on much longer timescales, Psyche's orbital and spin parameters will also vary, producing thermal waves that will propagate deeper into the subsurface. The north-south temperature asymmetry shown in Figure 2 is a result of the eccentricity (which determines the magnitude of asymmetry) and argument of perihelion (which controls which pole is warmer). As the spin pole precesses, the argument of perihelion will evolve, swapping which pole is warmer. So while our model predicts north-south temperature differences, we do not expect this to result in differences in volatile retention or thermal cracking over the long term.

In Section 3.2, we find that the large thermal stresses resulting from this orbital configuration could plausibly cause cracking and breakdown of large boulders. Our results agree with Hamm et al. (2019) that diurnal stress dominates in the equatorial regions. We also find that annual temperature variations may be more significant in the polar regions. Finite element modeling by Molaro et al. (2017) and El Mir et al. (2019) found that boulders comparable in size to the thermal skin depth are most susceptible to crack propagation and therefore eventual breakdown. On Psyche, this size dependence may be subverted if the boulders are a mixture of metal and silicates (which have different thermal expansivity). More work would be needed to understand how the superposition of these two periods and their respective skin depths would interact. We speculate that thermal cracking is a plausible source for a porous regolith, which would be consistent with the thermal inertial measurements (Appendix B). Other processes, such as impacts, may also contribute to regolith

production (Marchi et al. 2020). Because thermal cracking is only a surface-level process, we caution that the surface porosity and thermal inertia are likely not representative of the bulk porosity of Psyche.

5. Conclusions

In this work, our focus is on characterizing the surface temperatures at Psyche and their impact on the surface geology. We constructed a 1D thermal diffusion model that used an implicit solver and grid cells that increase in size with depth. This configuration allowed the model to resolve both diurnal and seasonal temperature variations. With this model, we found that because of Psyche's high obliquity, most of the surface experiences extremely large seasonal temperature variations (>100 K). Because of Psyche's large eccentricity, the mean temperature and temperature variations were asymmetric between the poles. We find that both diurnal and seasonal temperature variations may be large enough to cause crack propagation in surface boulders. These temperature variations may be responsible for a high-porosity surface regolith that would be consistent with existing thermal inertia measurements. Mean temperatures are high enough that we do not expect water ice to be stable anywhere in the near surface. Overall, we find that these large temperature variations may be an important geologic driver for the features observed by the Psyche spacecraft.

We thank two anonymous reviewers for their insightful comments. This work is supported by NASA contract NNM16AA09, "Psyche: Journey to a Metal World." Model outputs and plotting scripts can be found at <https://zenodo.org/record/5816194#.YdRxjtlBhE>.

Appendix A Variables Used

Table 1 lists all variables used throughout this work. Nominal values, or the range explored, are also provided.

Table 1
All Variables Used throughout This Work

Name	Symbol	Nominal Value (Range)	Units	Source
Stefan–Boltzmann constant	σ_{SB}	5.6704×10^{-8}	$\text{W m}^{-2} \text{K}^{-4}$	
Solar constant	S	1365	W m^{-2} (at 1 au)	
Thermal emissivity	ϵ	0.9	...	
Bond albedo	A	0.05	...	Matter et al. (2013); de Kleer et al. (2021)
Temperature	T		K	
Time	t		s	
Depth	z		m	
Model layer thickness	Δz		m	
Number of model layers	N			
Number of model layers with constant thickness	N_{surf}			
Model time step size	Δt	100	s	
Period	P		s	
Thermal forcing angular frequency	ω		s	
Thermal conductivity	k	0.02 (10 ⁻⁴ –1.0)	$\text{W m}^{-1} \text{K}^{-1}$	
Specific heat	c_p	500	$\text{J kg}^{-1} \text{K}^{-1}$	
Density	ρ	2000	kg m^{-3}	
Grain density	ρ_g	3800	kg m^{-3}	
Thermal inertia	Γ	100 (10–1000)	$\text{J m}^{-2} \text{K}^{-1} \text{s}^{-1/2}$ (tiu)	
Thermal diffusivity	κ		$\text{m}^2 \text{s}^{-1}$	
Thermal skin depth	δ		m	
Porosity	ϕ		...	
Porosity empirical parameter	a	4.1	...	Shoshany et al. (2002)
Porosity empirical parameter	b	0.22	...	Shoshany et al. (2002)
Porosity empirical parameter	ϕ_c	0.69	...	Shoshany et al. (2002)
Porosity empirical parameter	ϕ_{min}	0.01	...	Shoshany et al. (2002)
Stress	σ		Pa	
Elastic modulus	E	50×10^9	Pa	Hazeli et al. (2018)
Thermal expansivity	α	10 ⁻⁵	K ⁻¹	Delbo et al. (2014)
Paris law exponent	m	3.84	...	Delbo et al. (2014)
Paris law constant	C	3×10^{-4}	...	Delbo et al. (2014)
Integration constant	k_1		...	
Crack length	a		m	
Initial crack length	a_0		m	
Number of stress cycles	N		...	
Surface normal vector (components)	$N (N_x, N_y, N_z)$...	

Appendix B

The Connection between Thermal Inertia and Composition

The existing thermal inertia measurements have been used in part to make inferences about the composition of Psyche. Asteroids comparable in size have thermal inertias between 1 and 200 tiu (Capria et al. 2014; Delbo et al. 2015; Harris & Drube 2020). Matter et al. (2013) argued that their thermal inertia estimate for Psyche (123 ± 50 tiu) indicates that it is likely to be metallic in composition. Landsman et al. (2018) interpreted their low thermal inertia (15 ± 10 tiu) as favoring a silicate composition. These measurement have also been discussed in broader works reviewing Psyche’s likely composition (Elkins-Tanton et al. 2020). However, this connection is complicated by the strong dependence of thermal inertia on porosity. Here we examine the general relationship between thermal inertia, surface composition, and surface porosity.

On planetary bodies, porosity varies greatly on different scales. On the Moon, the near-surface porosity is $\gtrsim 50\%$ but decays rapidly within the first few tens of centimeters (Carrier et al. 1991; Hayne et al. 2017). In contrast, the Moon’s bulk crustal porosity in the upper tens of kilometers is 12% (Wieczorek et al. 2013). The thermal inertia measurements are only sensitive to the first few diurnal thermal skin depths

(~ 1 cm). For this reason, in this section, we will only focus on this very near surface regolith porosity. This surface porosity does not place a constraint on the bulk porosity needed to inform Psyche’s bulk composition (Elkins-Tanton et al. 2020; Shepard et al. 2021).

Lab measurements of thermal inertia for low-porosity ($<10\%$) meteorites have yielded values above 1000 tiu, and the thermal inertia of the iron meteorite Campo del Cielo is 8000 tiu (Yomogida & Matsui 1983; Opeil et al. 2010). The lowest reported thermal inertia of a meteorite is 644 tiu for a sample that has a porosity of 37% (Opeil et al. 2010). Empirical fits to these measurements are often used to infer the porosity of asteroid surfaces (Grott et al. 2019; Okada et al. 2020; Cambioni et al. 2021). These empirical fits, however, diverge for porosity values larger than $\sim 20\%$, the point at which the number of samples drops rapidly (Henke et al. 2016; Flynn et al. 2018; Grott et al. 2019). Given that Psyche’s inferred surface thermal inertia is significantly less than those measured in meteorites, we use physical scaling models to infer the surface porosity.

This order-of-magnitude difference between meteorite studies and Psyche’s surface requires a change of 2 orders of magnitude in the thermophysical properties (because of the

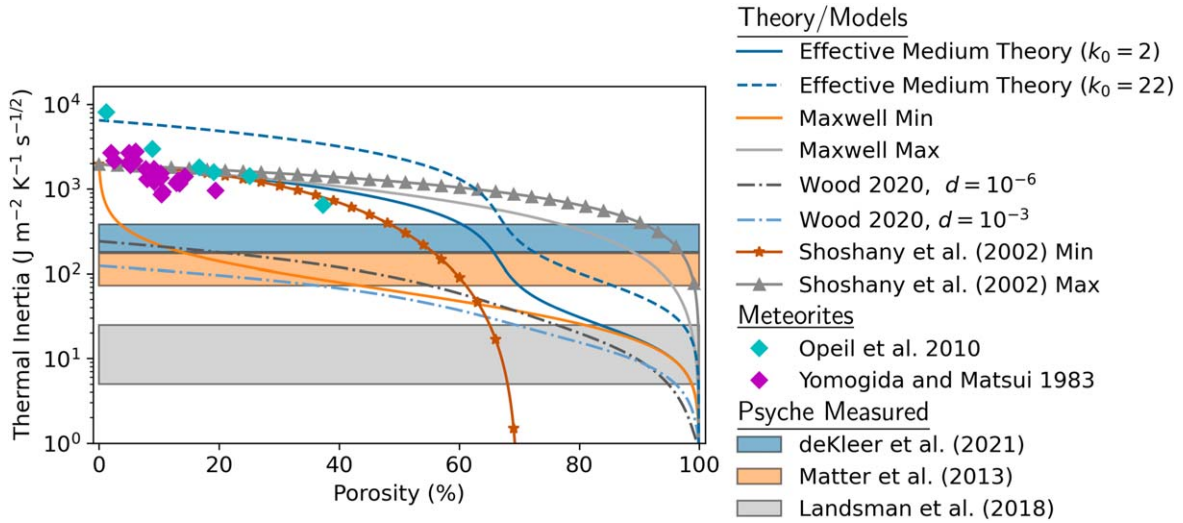


Figure 5. Psyche’s observed thermal inertia is significantly lower than meteorite samples and theoretical curves for low-porosity material. From this, we infer that Psyche’s surface likely has a very high porosity regolith. Psyche’s observed Γ is shown as shaded regions, meteorite measurements are diamonds, and theoretical curves are shown as lines. Model curves use base values of $k_0 = 2.0 \text{ W m}^{-1} \text{ K}^{-1}$, $k_r = 10^{-3} \text{ W m}^{-1} \text{ K}^{-1}$, $\rho_g = 3800 \text{ kg m}^{-3}$, and $c_p = 500 \text{ J kg}^{-1}$. Changing these bulk values would shift the lines vertically by the square root of the change (Equation (2)) but not change the dependence on porosity. This is shown by the two curves for effective medium theory, which use different solid thermal conductivity values. Meteorite thermal inertia values shown are all determined at 200 K.

square root in Equation (2)). A factor of 2 change in either c_p or ρ , which covers the range of likely materials, would only change the thermal inertia by a factor of 1.4. The most likely cause of this difference is surface porosity. Specific heat does not change as the porosity increases. However, both k and ρ decrease with increasing porosity. Density scales with the volume fraction as $\rho(\phi) = \rho_g(1 - \phi)$, where ρ_g is the grain density. The dependence of k on porosity is the strongest but also much more complex, as it depends on the structure and orientation of grains in addition to the ability of heat to be transferred through the porous gaps.

In a vacuum, heat transfer across the porous gaps occurs via radiation. This component is often estimated as an effective radiate conductivity (Wood 2020),

$$k_r = \frac{\epsilon}{2 - \epsilon} L 4 \sigma_{\text{SB}} T^3 \approx 10^{-3} \frac{\text{W}}{\text{mK}} \left(\frac{L}{10^{-3} \text{ m}} \right) \left(\frac{T}{200 \text{ K}} \right), \quad (\text{B1})$$

where L is the main length scale. Previous works equate L with either the grain size or the size of the pores between grains (Piqueux & Christensen 2009; Wood 2020). Because the radiative conductivity is significantly smaller than typical mineral conductivities, it only becomes important when conduction between grains is restricted.

We consider four parameterizations for the relationship between porosity and thermal conductivity. The first of these is the Maxwell model, which bounds the thermal conductivity of two mixed media. In this case, the thermal conductivity of the pores is the effective conductivity due to radiation transfer across pores, k_r . The bounds derived from the Maxwell model are (Carson et al. 2005)

$$k(\phi) = k_0 \frac{2k_0 + k_r - 2(k_0 - k_r)\phi}{2k_0 + k_r + (k_0 - k_r)\phi} \quad \text{minimum}, \quad (\text{B2})$$

$$k(\phi) = k_r \frac{2k_r + k_0 - 2(k_r - k_0)(1 - \phi)}{2k_r + k_0 + (k_r - k_0)(1 - \phi)} \quad \text{maximum}, \quad (\text{B3})$$

where k_0 is the conductivity of the solid material. For these bounds, it is assumed that only one medium is continuous. For the upper limit, the solid is continuous, and the pores are disconnected. For the lower limit, the pores are assumed to be continuous, and the solid is assumed to be disconnected. This lower limit is clearly not physically possible but serves as a useful mathematical bound.

Another analytic scaling is given by effective medium theory, which assumes the solid material and pores are arranged randomly, making it unbiased toward either phase (Carson et al. 2005):

$$k(\phi) = \frac{1}{4} \left((3\phi - 1)k_r + [3(1 - \phi) - 1]k_0 + \sqrt{[(3\phi - 1)k_r + (3(1 - \phi) - 1)k_0]^2 + 8k_r k_0} \right). \quad (\text{B4})$$

Two other instructive bounds are from the numerical work of Shoshany et al. (2002). That work used a fractal 3D Monte Carlo model and solved for the heat transfer in porous ice, including the effect of radiative heat transfer between grains. Shoshany et al. (2002) found minimum and maximum bounds on the heat transfer through a porous matrix,

$$k(\phi) = k_0(1 - \phi/\phi_c)^{a\phi+b} \quad \text{minimum}, \quad (\text{B5})$$

$$k(\phi) = k_0[(1 - \phi_{\text{min}}/\phi_c)^{a\phi_{\text{min}}+b}]^{\ln(1-\phi)/\ln(1-\phi_{\text{min}})} \quad \text{maximum}. \quad (\text{B6})$$

In these equations, the terms a , b , ϕ_c , and ϕ_{min} are all empirical parameters (see Table 1 for the values used). While this scaling was derived for use in cometary ice, the physics is the same in both systems. As shown in Figure 5, the lower bound of

Shoshany et al. (2002) roughly aligns with effective medium theory.

In a porous medium, grain size has a significant impact on the efficiency of heat transfer (Presley & Christensen 1997; Huetter et al. 2008; Piqueux & Christensen 2009; Sakatani et al. 2017, 2018; Ryan et al. 2020; Wood 2020; Ryan et al. 2022). The effect of grain size is primarily in changing the contact area between grains relative to their size (Wood 2020). While many studies have examined this effect in isolation, far fewer have put together models that include both the effects of porosity and grain size. This endeavor is complicated by the fact that porosity is itself a function of the grain size distribution and the shapes of those grains.

One model that does include both of these factors is that of Wood (2020). This model uses a weighting of the Maxwell limits described above (Equations (B2) and (B3)). This model includes additional parameters to describe the shapes of grains and the various factors influencing their contact area (including pressure, surface energy, and strength). Wood (2020) validated their model by comparing to experimental data with porosity values that range from 20% to 70%.

In Figure 5, we compare all of these models in the context of thermal inertia and compare them to estimates for Psyche's thermal inertia and lab measurements of meteorites. Higher-porosity meteorite samples do generally have a lower thermal inertia, as expected; however, all estimates for Psyche's thermal inertia are well below those measured in meteorite samples, particularly the iron meteorite Campo del Cielo, which has the highest thermal inertia of 8000 tti (Opeil et al. 2010).

A useful way to interpret all of these models is as mixing models between two end-members. At the low-porosity limit, heat transfer is controlled by solid conduction. All of the meteorite samples shown in Figure 5 are in this regime. At the high-porosity limit, radiative heat transfer is the dominant mechanism (this is the regime in which Psyche's thermal inertia estimates reside). Radiative heat transfer itself also depends on the porosity (Ryan et al. 2020, 2022; Wood 2020), but more important in this context is determining at what porosity the transition between these regimes occurs.

If we consider the lower bound of Shoshany et al. (2002) or effective medium theory, the implied porosity of Psyche's surface is greater than ~60% regardless of which thermal inertia estimate is correct. The lower bound of the Maxwell model varies from 5% to 44% when compared to the Matter et al. (2013) and de Kleer et al. (2021) thermal inertia estimates. This curve, however, both is physically impossible (as it assumes that no grains are in contact) and does not match the low-porosity meteorite data.

If we instead focus on the curves in Figure 5 corresponding to the model of Wood (2020), it appears that much lower porosity may be allowed. It is important to observe, however, that the curves of Wood (2020) do not converge to the correct limit at 0% porosity (where the conductivity should be that of the solid). It is not clear at what porosity the model of Wood (2020) becomes valid. One choice is to trust it for $\phi > 20\%$, where it was compared to experimental data. However, in this range, it still significantly underestimates the thermal inertia when compared to the meteorite studies of Yomogida & Matsui (1983) and Opeil et al. (2010).

In summary, the low thermal inertia of Psyche strongly implies a very porous surface, regardless of composition. This is in part due to the lack of robust models that characterize the

porosity of the transition between solid conduction and radiative heat transfer. Because the thermal inertia is so sensitive to this unknown porosity, no strong statements can be made using thermal inertia to infer the surface composition.

Appendix C Model Verification

To evaluate the required “spin-up” time and assess the accuracy of our thermal diffusion solver, we compare it to the analytic solution for a cyclically varying surface temperature. To best mimic the conditions of Psyche, we force the surface with two sinusoidal periods. The surface temperature is given by

$$T_s = \bar{T} + \Delta T_d \cos(\omega_d t) + \Delta T_a \cos(\omega_a t). \quad (C1)$$

Assuming no basal heat flux, the solution for the temperature with depth is given by Turcotte & Schubert (2014):

$$T(z) = \bar{T} + \Delta T_d \cos(\omega_d t - z/\delta_d) e^{-z/\delta_d} + \Delta T_a \cos(\omega_a t - z/\delta_a) e^{-z/\delta_a}. \quad (C2)$$

We start the model with a constant initial temperate that is 10 K higher than \bar{T} , comparable to the estimated error in our full model. We use two metrics to evaluate the model runs, the rms error in the top 1 cm, and the rms error in the bottom 1 m. These quantify how well the model is resolving near-surface variations and long-term means.

Figure 6 shows the rms error in the upper diurnal (panel (a)) and bottom annual skin depths (panel (b)). Within the first diurnal skin depth, the system equilibrates within the first year. After that, the rms error in this region stays below 0.5 K. The bottom annual skin depth in the model domain (which is $8\delta_a$ deep) takes much longer to equilibrate.

Figure 6 shows the rms temperature error as a function of depth. In the upper meter (Figure 6(a)), the temperature errors are less than 2 K. This is small when compared to the mean temperature of 150 K and temperature variation of 50 K (Table 2). These subsurface temperatures can impact the surface temperatures via the geothermal flux (Equation (12)). Because the focus of this work is surface temperatures, the error in the geothermal flux is the key quantity we need to minimize.

Figure 7 shows the error in the surface flux for the same analytic test. This figure shows that the surface flux error is $< 3 \text{ W m}^{-2}$ after the initialization. For comparison, at Psyche's orbit, the solar insolation is $\sim 160 \text{ W m}^{-2}$. This error might be expected to have the largest impact in polar winter when the stored thermal energy buffers the surface temperatures. Typical model fluxes for polar winter are $\sim 5 \text{ W m}^{-2}$. Raising them to 8 W m^{-2} would change the surface temperature by $\sim 10 \text{ K}$. We also performed an analytic comparison with only an annual forcing ($\Delta T_d = 0$) shown in Figure 7. In this case, the error in the surface flux is $\ll 1 \text{ W m}^{-2}$ and would have no notable influence on our results.

The results of this work focus on the temperatures at the surface and in the upper meter. As described in Section 3, changing the surface thermal properties changes the mean temperature by tens of kelvins. From these tests, we estimate that the numerical errors are of order a few kelvins, much smaller than the range of results acquired for different thermal properties.

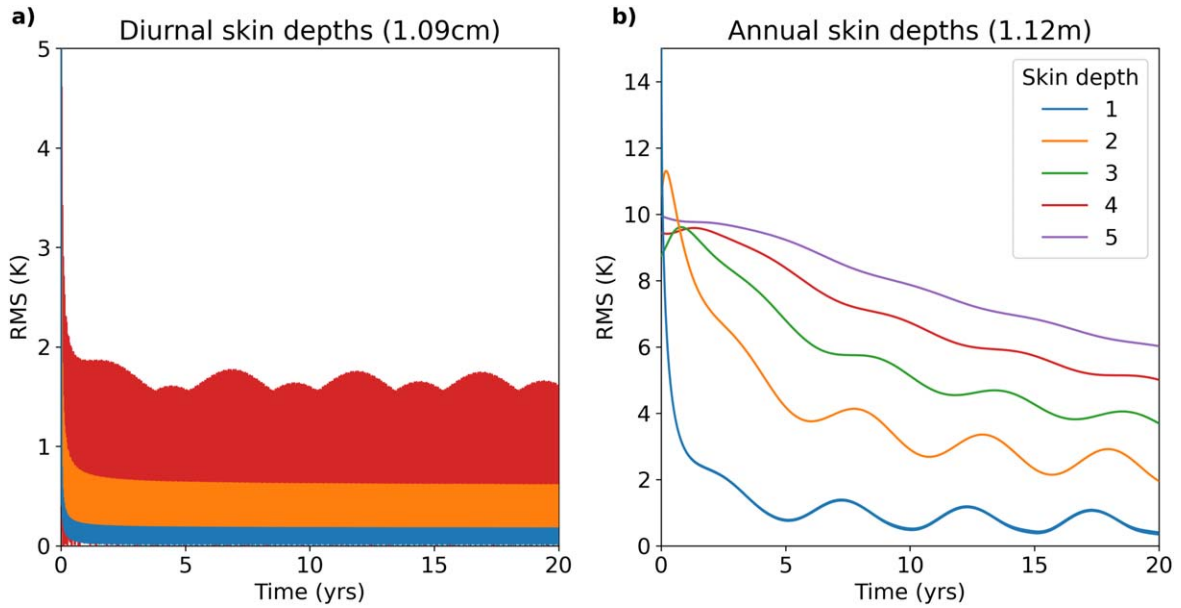


Figure 6. The rms error in the upper five diurnal skin depths (panel (a)) and annual skin depth (panel (b)). In the near surface, the error between three and four diurnal skin depths is larger than that at four to five skin depths (so the latter is not visible). For reference, all results presented in the main text have been initialized for three orbits (~ 15 yr).

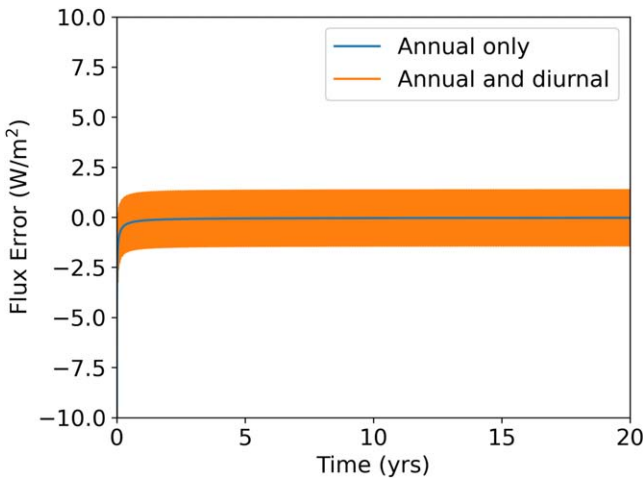


Figure 7. Error in the surface flux for the sin test. Results are shown that include both the annual and diurnal periods and those that only include the annual period (similar to the real polar forcing).

Table 2
Parameters Used for Analytic Test of Model

\bar{T}	150 K
T_0	140 K
ΔT_d	50 K
ΔT_a	20 K
ω_d	$2\pi/4.1$ hr
ω_a	$2\pi/5$ yr

C.1. Comparison to Other Model Configurations

Many thermal models for asteroids exist in the literature (Emery et al. 2006; Matter et al. 2011; Delbo et al. 2015; Hanuš et al. 2018). The focus of these models is generally on reproducing Earth-based thermal observations. While specific details can vary, it is common for such models to

nondimensionalize the depth and time by the diurnal skin depth and rotation period of the asteroid. Typical model domains are about 10 diurnal skin depths deep and initialized for hundreds of rotations (Delbo et al. 2015). In contrast, in this work, we use eight annual skin depths and initialize for three orbits.

To demonstrate the differences inherent in these approaches, we use our model with parameters that replicate standard asteroid thermophysical models (TPMs; Delbo et al. 2015). For this “standard TPM” parameter set, we use 40 vertical grid points extending eight diurnal skin depths. We use an Euler explicit solver and CFL time step. This case is run for 100 Earth days (10^5 steps) before comparing to our nominal case. For this comparison, we used an ideal sphere (not Psyche’s shape) to isolate the impact of the model configuration.

What we find in this comparison (Figure 8) is that for regions in standard illumination (Sun setting and rising) or polar day, there is very little difference between the two cases (< 1 K). However, for regions in polar night, there can be differences of more than 10 K. It is also very important to note that the size of this difference depends on the initial temperature of the standard TPM case.

The reason for this difference is fairly straightforward. During polar night, the surface temperature is maintained by heat conducted from the seasonal skin depth below the surface. Because the standard TPM case is not run long enough to initialize this heat from the previous polar summer and does not have a deep enough model domain to store that heat even if it was, it cannot accurately model temperatures during polar night.

It is important to note again the standard use for standard TPM models in this context. Because of the small phase angles Psyche has been viewed at, regions in polar night make up a tiny (or nonexistent) fraction of the observed surface area. For this reason, these models are well suited to characterize their surface temperatures as viewed from Earth. They are not well suited, however, for determining surface temperatures in polar night.

Northern Summer

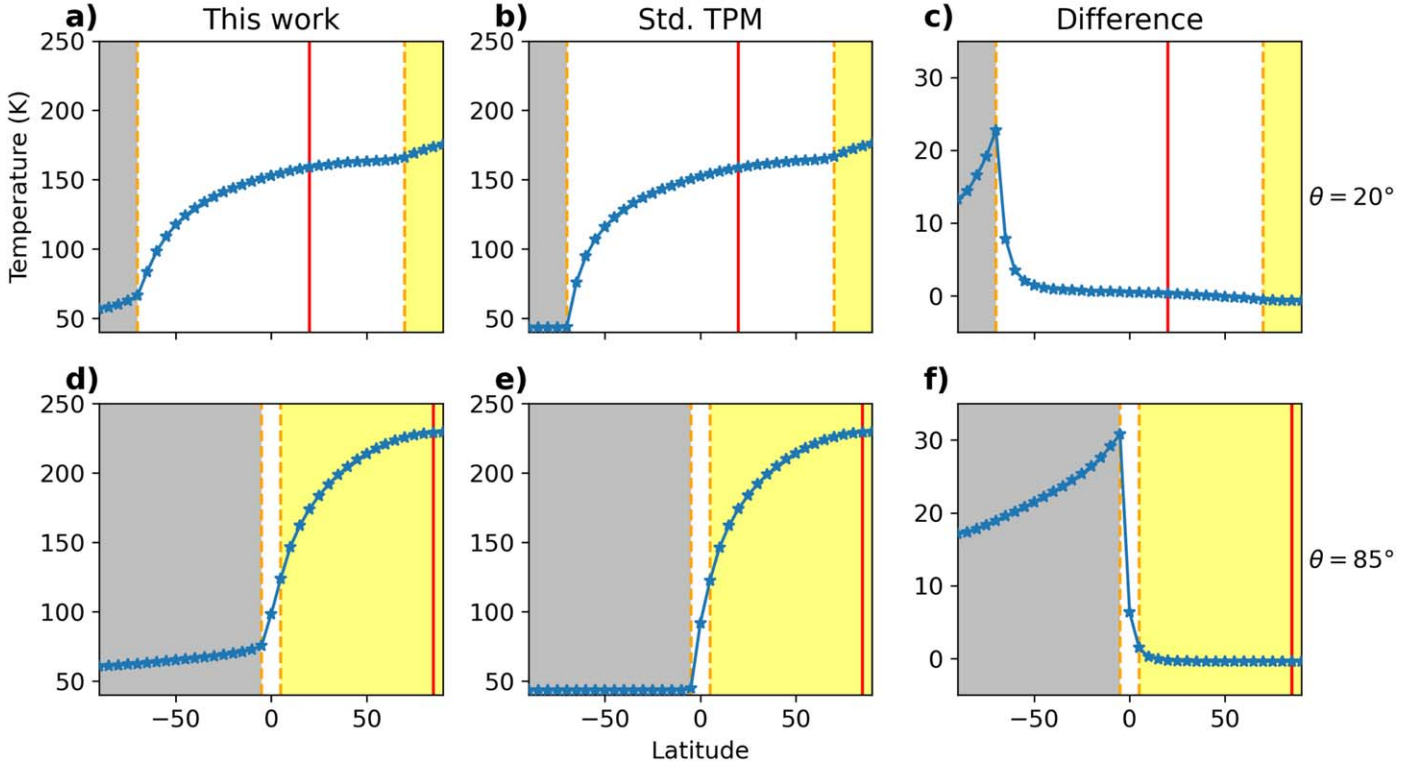


Figure 8. A deep model domain is important for realistically modeling surface temperatures during polar night. We compare the model used in this work with the standard TPM configuration. This configuration uses a shallow model domain (eight diurnal skin depths), and the object is fixed in its orbit as it rotates. The top row are models with an obliquity of 20° , and the bottom row is for 85° . In each plot, the vertical red line is the subsolar latitude at the time of this snapshot. Regions shaded yellow are in polar day, and regions shaded gray are in polar night. For this example, no shape model is used (assumed perfect sphere).

Appendix D Derivation of Paris Equation Integration

In this section, we derive Equation (16). We begin with the Paris equation,

$$\frac{da}{dN} = C(\Delta\sigma\sqrt{\pi a})^m, \quad (D1)$$

$$\frac{da}{dN} = C(\Delta\sigma\sqrt{\pi})^m a^{m/2}, \quad (D2)$$

$$\frac{a^{1-m/2}}{1-m/2} = C(\Delta\sigma\sqrt{\pi})^m N + k_1, \quad (D3)$$

$$a(N) = [(1-m/2)(C(\Delta\sigma\sqrt{\pi})^m N + k_1)]^{1/(1-m/2)}. \quad (D4)$$

We can then solve for the integration constant, k_1 , by setting $a(0) = a_0$:

$$a(0) = a_0 = [(1-m/2)(k_1)]^{1/(1-m/2)}, \quad (D5)$$

$$\frac{a_0^{1-m/2}}{1-m/2} = k_1, \quad (D6)$$

$$a(N) = \left[(1-m/2) \left(C(\Delta\sigma\sqrt{\pi})^m N + \frac{a_0^{1-m/2}}{1-m/2} \right) \right]^{1/(1-m/2)}, \quad (D7)$$

$$a(N) = [(1-m/2)C(\Delta\sigma\sqrt{\pi})^m N + a_0^{1-m/2}]^{1/(1-m/2)}. \quad (D8)$$

If we define N_{crit} as

$$N_{\text{crit}} = \frac{-a_0^{1-m/2}}{(1-m/2)C(\Delta\sigma\sqrt{\pi})^m}, \quad (D9)$$

we can substitute N_{crit} into Equation (D8), and it becomes

$$a(N) = a_0 \left[1 - \frac{N}{N_{\text{crit}}} \right]^{1/(1-m/2)}. \quad (D10)$$

In this form, as discussed in the main text, it can be seen that when $N \ll N_{\text{crit}}$, the crack length is nearly constant ($a(N) \approx a_0$). When $N \geq N_{\text{crit}}$, the crack grows as a power law.

Appendix E Cracking with Diurnal Temperature Variations

To calculate the diurnal temperature variations, during model runs, temperatures for the last rotational period are stored. The diurnal temperature variation is taken to be the difference between the maximum and minimum temperatures for each location. This estimate is an upper limit, as it will also include some component as the annual thermal wave.

While N_{crit} (Equation (17)) is well defined for a constant temperature variation, a slightly altered criterion is needed due to the fact that diurnal temperature variations change seasonally (Figure 9). We therefore estimate N_{crit} for diurnal temperatures

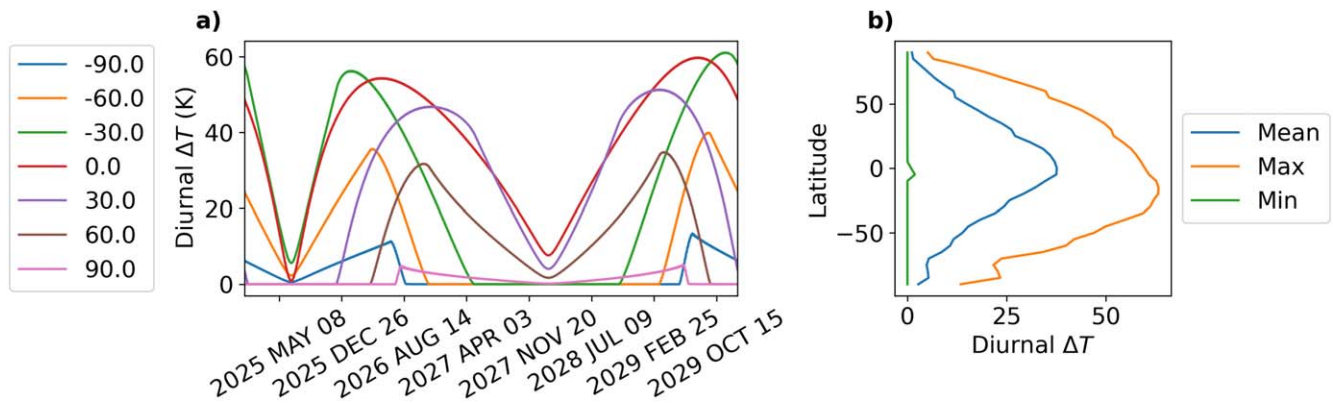


Figure 9. As expected, the diurnal temperature variations are strongest in the equatorial region. Generally, diurnal temperature variations are a factor of 2–5 times weaker than annual temperature variations. (a) Diurnal temperature variations as a function of season and latitude. (b) Maximum, minimum, and mean diurnal temperature variation as a function of latitude.

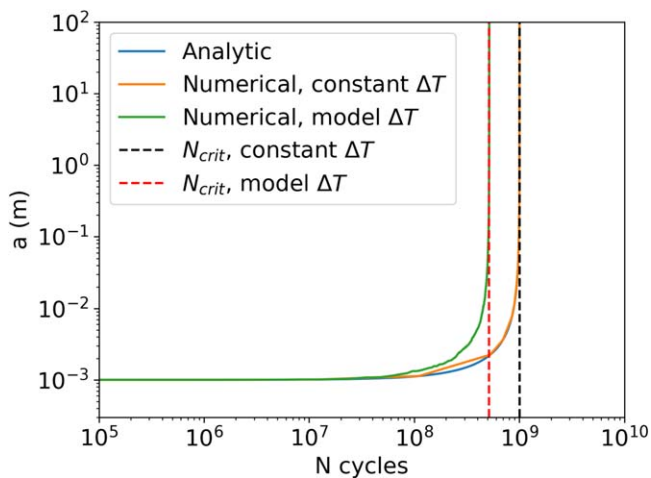


Figure 10. Comparison of numerically integrating the Paris law (Equation (14)) with a diurnal temperature variation history, constant temperature variation, and the constant temperature analytic solution (Equation (16)). The value for N_{crit} is shown by the vertical dashed lines. When the numerical method is given a constant ΔT , it recovers the analytic solution for N_{crit} to within 0.1%. Integrating with the model diurnal ΔT results in a slightly smaller N_{crit} than using the analytic scaling for the seasonal mean of the diurnal ΔT . This difference is expected, as the crack growth is a power law with ΔT .

as the point when the crack length a exceeds 1 m. The choice of 1 m is arbitrary, but the results are not sensitive to the choice so long as it is much larger than the initial crack size. This independence from the final crack length is shown in Figure 10, where the crack size is shown to be nearly constant until growing rapidly over several orders of magnitude. We find that, using a constant temperature variation, this approach finds the value of N_{crit} defined by Equation (17) within 0.1%.

ORCID iDs

Carver J. Bierson <https://orcid.org/0000-0002-6840-7187>
 Linda T. Elkins-Tanton <https://orcid.org/0000-0003-4008-1098>
 Joseph G. O'Rourke <https://orcid.org/0000-0002-1180-996X>

References

Acton, C., Bachman, N., Semenov, B., & Wright, E. 2016, SPICE tools supporting planetary remote sensing, JPL, NASA, <https://trs.jpl.nasa.gov/handle/2014/46088>

- Annex, A. M., Pearson, B., Seignovet, B., et al. 2020, *JOSS*, **5**, 2050
 Becker, T. M., Cunningham, N., Molyneux, P., et al. 2020, *PSJ*, **1**, 53
 Cambioni, S., de Kleer, K., & Shepard, M. 2022, *JGRE*, **127**, e07091
 Cambioni, S., Delbo, M., Poggiali, G., et al. 2021, *Natur*, **598**, 49
 Capria, M. T., Tosi, F., De Sanctis, M. C., et al. 2014, *GeoRL*, **41**, 1438
 Carrier, W. D., III, Olhoeft, G. R., & Mendell, W. 1991, in *Lunar Sourcebook, A User's Guide to the Moon*, ed. B. M. French, D. Vaniman, & G. Heiken (Cambridge: Cambridge Univ. Press), 475
 Carson, J. K., Lovatt, S. J., Tanner, D. J., & Cleland, A. C. 2005, *IJHMT*, **48**, 2150
 Collins, B. D., & Stock, G. M. 2016, *NatGe*, **9**, 395
 de Kleer, K., Cambioni, S., & Shepard, M. 2021, *PSJ*, **2**, 149
 Delbo, M., Libourel, G., Wilkerson, J., et al. 2014, *Natur*, **508**, 233
 Delbo, M., Mueller, M., Emery, J. P., Rozitis, B., & Capria, M. T. 2015, in *Asteroids IV*, ed. P. Michel, F. E. DeMeo, & W. F. Bottke (Tucson, AZ: Univ. Arizona Press), doi:10.2458/azu_uapress_9780816532131-ch006
 Dobrovolskis, A. R. 2021, *Icar*, **363**, 114297
 El Mir, C., Ramesh, K. T., & Delbo, M. 2019, *Icar*, **333**, 356
 Elkins-Tanton, L. T., Asphaug, E., Bell, J. F., III, et al. 2020, *JGRE*, **125**, e06296
 Emery, J., Cruikshank, D., & Van Cleve, J. 2006, *Icar*, **182**, 496
 Flynn, G. J., Consolmagno, G. J., Brown, P., & Macke, R. J. 2018, *ChEG*, **78**, 269
 Grott, M., Knollenberg, J., Hamm, M., et al. 2019, *NatAs*, **3**, 971
 Haddar, N., Fissolo, A., & Maillot, V. 2005, *IJS*, **42**, 771
 Hamm, M., Senshu, H., & Grott, M. 2019, *Icar*, **319**, 308
 Hanuš, J., Delbo, M., Durech, J., & Alí-Lagoa, V. 2018, *Icar*, **309**, 297
 Harris, A. W., & Drube, L. 2020, *ApJ*, **901**, 140
 Hayne, P. O., Bandfield, J. L., Siegler, M. A., et al. 2017, *JGRE*, **122**, 2371
 Hazeli, K., El Mir, C., Papanikolaou, S., Delbo, M., & Ramesh, K. T. 2018, *Icar*, **304**, 172
 Henke, S., Gail, H.-P., & Tieloff, M. 2016, *A&A*, **589**, A41
 Huetter, E. S., Koemle, N. I., Kargl, G., & Kaufmann, E. 2008, *JGRE*, **113**, E12004
 Janssen, M., Zuidema, J., & Wanhill, R. J. H. 2002, *Fracture Mechanics: Fundamentals and Applications* (London: Taylor & Francis) <https://doi.org/10.1201/9781482265583>
 Johnson, B. C., Sori, M. M., & Evans, A. J. 2020, *NatAs*, **4**, 41
 Kieffer, H. 2013, *JGRE*, **118**, 451
 Landsman, Z. A., Emery, J. P., Campins, H., et al. 2018, *Icar*, **304**, 58
 Libourel, G., Ganino, C., Delbo, M., et al. 2021, *MNRAS*, **500**, 1905
 MacLennan, E., Toliou, A., & Granvik, M. 2021, *Icar*, **366**, 114535
 Marchi, S., Durda, D. D., Polanskey, C. A., et al. 2020, *JGRE*, **125**, e05927
 Matter, A., Delbo, M., Carry, B., & Ligori, S. 2013, *Icar*, **226**, 419
 Matter, A., Delbo, M., Ligori, S., Crouzet, N., & Tanga, P. 2011, *Icar*, **215**, 47
 Migliazza, M., Ferrero, A. M., & Spagnoli, A. 2011, *International Journal of Rock Mechanics and Mining Sciences*, **48**, 1038
 Molaro, J., Byrne, S., & Le, J.-L. 2017, *Icar*, **294**, 247
 Molaro, J. L., Walsh, K. J., Jawin, E. R., et al. 2020, *NatCo*, **11**, 2913
 Okada, T., Fukuhara, T., Tanaka, S., et al. 2020, *Natur*, **579**, 518
 Opeil, C., Consolmagno, G., & Britt, D. 2010, *Icar*, **208**, 449
 Paige, D. A., Wood, S. E., & Vasavada, A. R. 1992, *Sci*, **258**, 643
 Piqueux, S., & Christensen, P. R. 2009, *JGRE*, **114**, E09006
 Presley, M. A., & Christensen, P. R. 1997, *JGR*, **102**, 6535

- Putzig, N. E. 2006, PhD thesis, Univ. Colorado <https://search.proquest.com/openview/9555f31cc9ba610b9c0d486d00dbf610/1?pq-origsite=gscholar&cbl=18750&diss=y>
- Ravaji, B., Alí-Lagoa, V., Delbo, M., & Wilkerson, J. W. 2019, *JGRE*, **124**, 3304
- Rozitis, B., Emery, J. P., Siegler, M. A., et al. 2020, *JGRE*, **125**, e06323
- Ryan, A. J., Pino Muñoz, D., Bernacki, M., et al. 2022, *JGRE*, **127**, e07191
- Ryan, A. J., Pino Muñoz, D., Bernacki, M., & Delbo, M. 2020, *JGRE*, **125**, e06100
- Sakatani, N., Ogawa, K., Arakawa, M., & Tanaka, S. 2018, *Icar*, **309**, 13
- Sakatani, N., Ogawa, K., Iijima, Y., et al. 2017, *AIPA*, **7**, 015310
- Schorghofer, N. 2008, *ApJ*, **682**, 697
- Schorghofer, N. 2016, *Icar*, **276**, 88
- Schörghofer, N., & Hsieh, H. H. 2018, *JGRE*, **123**, 2322
- Schorghofer, N., & Taylor, G. J. 2007, *JGRE*, **112**, E02010
- Shepard, M. K., Kleer, K. d., Cambioni, S., et al. 2021, *PSJ*, **2**, 125
- Shepard, M. K., Richardson, J., Taylor, P. A., et al. 2017, *Icar*, **281**, 388
- Shoshany, Y., Prialnik, D., & Podolak, M. 2002, *Icar*, **157**, 219
- Spencer, J. R., Lebofsky, L. A., & Sykes, M. V. 1989, *Icar*, **78**, 337
- Turcotte, D. L., & Schubert, G. 2014, *Geodynamics* (Cambridge: Cambridge Univ. Press)
- Vokrouhlický, D., Bottke, W. F., Chesley, S. R., Scheeres, D. J., & Statler, T. S. 2015, in *Asteroids IV*, ed. P. Michel, F. E. DeMeo, & W. F. Bottke (Tucson, AZ: Univ. Arizona Press), 509
- Ward, W. R. 1974, *JGR*, **79**, 3375
- Watson, K., Murray, B. C., & Brown, H. 1961, *JGR*, **66**, 3033
- Wieczorek, M. a., Neumann, G. a., Nimmo, F., et al. 2013, *Sci*, **339**, 671
- Wood, S. E. 2020, *Icar*, **352**, 113964
- Yomogida, K., & Matsui, T. 1983, *JGR*, **88**, 9513